Rafiul Shihab
Department of Mechanical Engineering,
University of Nevada, Reno,
Reno, NV 89557-0312
e-mail: rhshihab@nevada.unr.edu

Tasmirul Jalil
Department of Mechanical Engineering,
University of Nevada, Reno,
Reno, NV 89557-0312
e-mail: mjalil@nevada.unr.edu

Burak Gulsacan
Department of Mechanical Engineering,
University of Nevada, Reno,
Reno, NV 89557-0312
e-mail: bgulsacan@nevada.unr.edu

Matteo Aureli
Department of Mechanical Engineering,
University of Nevada, Reno,
Reno, NV 89557-0312
e-mail: maureli@unr.edu

Ryan Tung[1]
Department of Mechanical Engineering,
University of Nevada, Reno,
1664 N. Virginia Street,
Reno, NV, 89557-0312
e-mail: rtung@unr.edu

Sensor Egregium—An Atomic Force Microscope Sensor for Continuously Variable Resonance Amplification

Numerous nanometrology techniques concerned with probing a wide range of frequency-dependent properties would benefit from a cantilevered sensor with tunable natural frequencies. In this work, we propose a method to arbitrarily tune the stiffness and natural frequencies of a microplate sensor for atomic force microscope applications, thereby allowing resonance amplification at a broad range of frequencies. This method is predicated on the principle of curvature-based stiffening. A macroscale experiment is conducted to verify the feasibility of the method. Next, a microscale finite element analysis is conducted on a proof-of-concept device. We show that both the stiffness and various natural frequencies of the device can be controlled through applied transverse curvature. Dynamic phenomena encountered in the method, such as eigenvalue curve veering, are discussed and methods are presented to accommodate these phenomena. We believe that this study will facilitate the development of future curvature-based microscale sensors for atomic force microscopy applications. [DOI: 10.1115/1.4050274]

Keywords: dynamics, sensors and actuators, system identification, vibration control

1 Introduction

Several atomic force microscope (AFM) contact imaging modes measure small surface displacements at specific excitation frequencies. For instance, scanning Joule expansion microscopy (SJEM) is used to measure the local thermal expansion of a sample of interest due to Joule (and other forms of) heating. SJEM has been used to measure the thermal conductivity of metal thin films [1] and single-walled carbon nanotubes [2] to enhance the performance of microelectronic and nanoelectronic systems. SJEM has also been used to study the energy storage capability of various strains of *Streptomyces* bacteria, by studying oil inclusions in the microorganism, to enhance the production of biodiesel fuels [3]. Piezoresponse force microscopy (PFM) is used to study piezoelectric and ferroelectric domains through the application of an oscillating electric field [4] and surface displacement measurements. Finally, electrochemical strain microscopy (ESM) measures surface deformations due to ionic flows in a material and has been used to study electrochemical processes in various materials [5–7] to enhance energy generation and storage in applications such as batteries and fuel cells.

To increase the signal to noise ratio (SNR) and improve the measurement of small surface displacements, the field of contact resonance (CR) spectroscopy [8–14] has garnered ever-increasing attention in the AFM community. CR spectroscopy uses the measurement of the natural frequencies of vibration of the permanently coupled tip–sample system and resonance amplification to obtain quantitative information about the sample. It follows naturally that CR spectroscopy techniques would be combined with the aforementioned advanced contact modes of AFM. For example, coupling CR methods with PFM [15–17] has shown drastic measurement enhancement due to resonance amplification. However, one primary issue with current CR methods is that the amplification bandwidth of the measurement is constrained to the bandwidth of the discrete natural frequencies of the system. That is, one can only measure frequency-dependent phenomena, with resonance amplification, in very small frequency windows. Additionally, changes in sample topography and material properties can alter the locations of these natural frequencies.

One way to achieve resonance amplification at arbitrary frequencies is to adjust the stiffness of the sensor in situ. Mechanical methods for in situ stiffness adjustment include: changing the effective length of the resonating beam structure [18–20], utilizing thermal input to impose thermal stresses [21] on the structure or affect the temperature-dependent Young's modulus [22], and changing the shape of the device to adjust the stiffness. For example, Kawai et al. [23] used a complex device geometry with piezoelectric elements to fold a microelectromechanical system beam, thereby changing the beam's second area moment, effectively changing the device stiffness. This device achieved a 14% change in static stiffness between the folded and unfolded states.

We posit that a continuous plate geometry utilizing curvature induced in-plane straining will allow in situ static and dynamic stiffness adjustment across a wide range of frequencies while simultaneously offering increased sensor bandwidth [24]. This idea originates from the *Theorema Egregium* of C. F. Gauss [25] who showed that, under a local isometry, the Gaussian curvature of a surface is invariant, where the Gaussian curvature is the product of the two principal curvatures of the surface. In other words, the initial Gaussian curvature of a surface remains the same under a transformation that does not result in stretching or compressing of the material. Uniaxial bending of a narrow beam undergoing small displacement is an example of such a transformation. However, a plate undergoing biaxial bending necessarily produces in-plane straining. This can be achieved by first applying a transverse curvature to the plate and then bending the plate in an axis

[1]Corresponding author.
Contributed by the Technical Committee on Vibration and Sound of ASME for publication in the Journal of Vibration and Acoustics. Manuscript received October 22, 2020; final manuscript received February 9, 2021; published online March 10, 2021. Assoc. Editor: Slava Krylov.

orthogonal to the applied curvature. Pini et al. [26] have shown that the stiffness of cantilevered plates undergoing flexural bending is significantly increased due to in-plane straining caused by an initially applied transverse curvature.

In this work, we explore the idea of a curvature-based stiffening sensor for AFM applications and christen such a system as "Sensor Egregium"—the namesake of the Theorema Egregium. The remainder of the paper is organized as follows. In Sec. 2, a proof-of-concept macroscale experiment is conducted to investigate the feasibility of the principle. Next, in Sec. 3, a microscale finite element analysis of a proof-of-concept microplate sensor, using piezoelectric materials to apply curvature, is conducted. In Sec. 4, we analyze the effect that applied transverse curvature has on the microplate static stiffness and natural frequencies. An eigenfunction sensitivity method is presented in order to accurately track mode shapes of interest, and an analysis is performed to study the performance effect that the applied curvature has on contact resonance AFM measurements using the proof-of-concept sensor. We believe this work represents the first proof-of-concept microplate sensor utilizing applied transverse curvature to actively manipulate the device stiffness and resonant frequencies. Additionally, we show that complicated dynamic behaviors, such as eigenfrequency curve veering, are observed in this device as curvature is applied and offer techniques to accommodate these behaviors.

2 Concept of Curvature Stiffening

Here, we investigate a new sensor geometry to sensitively detect surface deformations at arbitrary frequencies, as schematically depicted in Fig. 1. As explained by Pini et al. [26], biaxial bending of thin plates generates in-plane straining which increases the total elastic energy of the system and thus increases the effective stiffness of the system. For a thin, homogeneous plate fixed at one edge with applied static curvatures in the longitudinal and transverse directions, Pini et al. [26] reported a relationship which describes the relative change of the stiffness of the system $\Delta k/k$ subject to longitudinal bending:

$$\frac{\Delta k}{k} = C\frac{b^4}{h^2}\left(\kappa_y - \nu\kappa_x\right)^2 \tag{1}$$

where C is a constant that depends on the mode shape and geometry of the plate, b is the width of the plate, h is the thickness of the plate, κ_y is the curvature in the y-direction of the plate (width direction), κ_x is the curvature in the x-direction of the plate (length direction), and ν is Poisson's ratio of the plate material. To derive this equation the following assumptions have been made: (i) the deformation is symmetric about the y-axis, (ii) the y-direction curvature of the static and dynamic z-displacement does not depend on the y-coordinate, and (iii) the plate is comprised of an isotropic material. After inducing curvature on the structure, the elastic strain energy of the system is calculated. Utilizing Euler–Lagrange equations, and by neglecting higher order terms, four differential equations can be formulated and solved, and the solution can be used to calculate the relative change of stiffness, and resonance frequency, leading to the derivation of Eq. (1). For further details the reader should consult Ref. [26] and its supplementary material. From this relationship, we see that the stiffening effect is primarily governed by the width of the plate, relative to its thickness, and the applied transverse curvature. The particular mode shape of vibration also controls the magnitude of the curvature stiffening effect, as will be discussed in Sec. 4.

2.1 A Proof-of-Concept Experiment. To investigate the effect of imposed transverse curvature on the vibration characteristics of a cantilevered plate at the macroscale, we conduct experiments on a prototype system comprised of a carbon steel (AISI 1080) plate with a total length of $L_T = 154$ mm, free length $L = 104$ mm, width $b = 104$ mm, and thickness $h = 0.254$ mm as shown in Fig. 2(*a*). We also assume Young's modulus and Poisson's ratio of AISI 1080 to be 200 GPa and 0.3, respectively. The term "free length" indicates the part of the plate that is free to vibrate and not constrained by the clamp that is used to create the fixed boundary condition. Specifically, the test plate is located between two rigid aluminum plates, each with a thickness of 3 mm, to ensure proper cantilevered boundary conditions. This assembly is connected to a Vibration Research VR520 shaker which provides base excitation to the cantilever steel plate, see Fig. 2(*b*). A Rigol DG1022 function generator is used to regulate the excitation of the plate. The signal from the function generator is amplified using a Vibration Research VR565 amplifier.

A bi-morph actuator is constructed from two Macro-Fiber Composite (MFC) actuators, model M8528-P1, procured from Smart Material Corp. and bonded to the plate at the free end. The bi-morph actuator is controlled via an AMD2012-CE amplifier, procured from Smart Material Corp., driven by a low voltage signal produced by a National Instrument USB-6341 DAQ card, operated via a custom VI in LABVIEW. To induce transverse curvature in the cantilevered plate, the bi-morph actuator uses piezoelectric strips which operate in the d22 mode to expand in the direction of

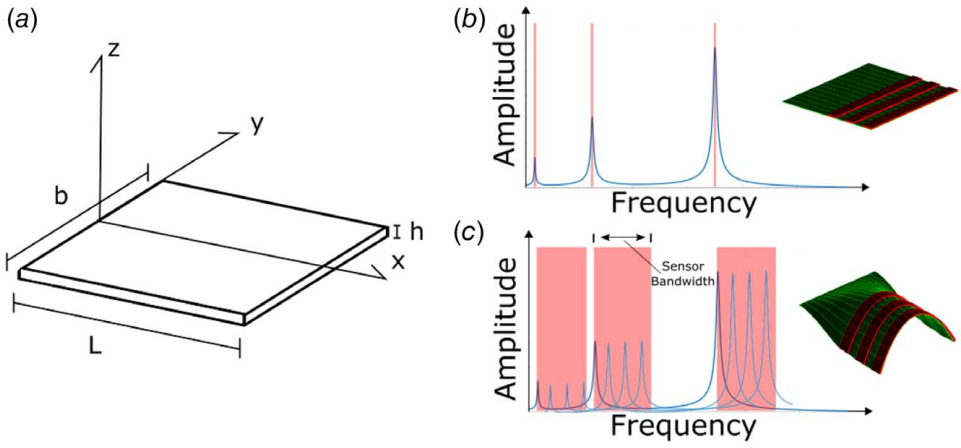

Fig. 1 (*a*) Proposed AFM sensor in its unperturbed state with width *b*, length *L*, and thickness *h*. (*b*) The natural frequencies of the unperturbed device are shown on the amplitude versus frequency plot. (c) As transverse curvature is applied, the natural frequencies of the device increase. The location of the natural frequencies of vibration of the sensor can be controlled through applied transverse curvature. The inset of (*b*) and (c) represents the plate sensor before and after the transverse curvature is applied, respectively.

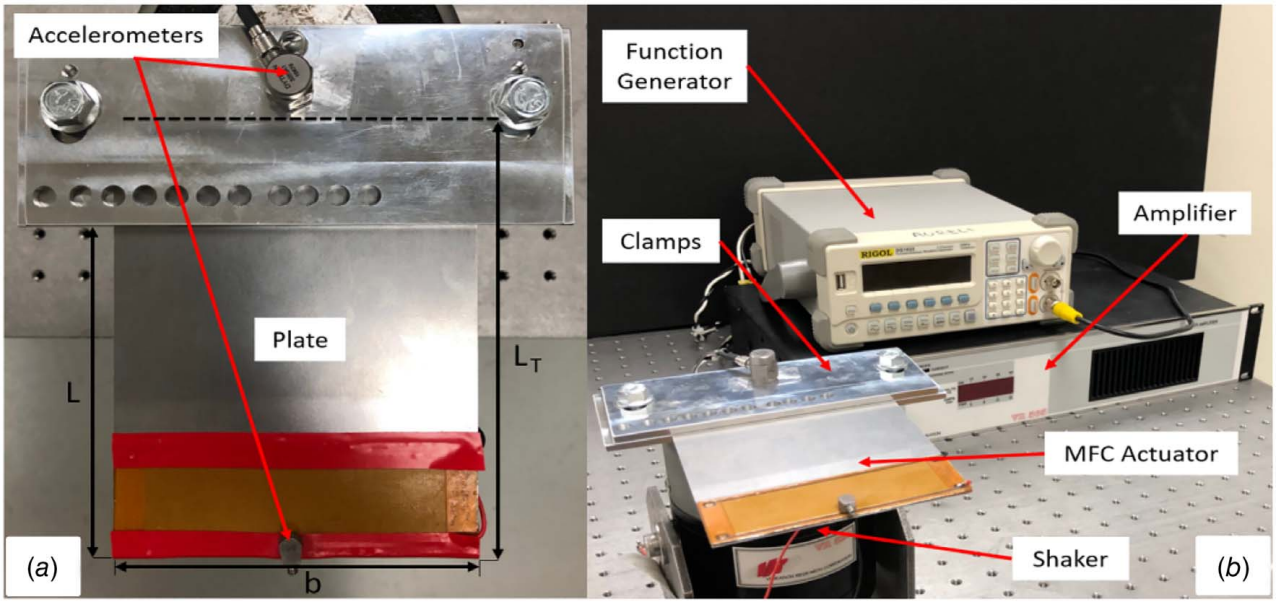

Fig. 2 (*a*) Test plate and accelerometers with MFC bi-morph actuator at the free end. The primary plate dimensions are indicated. (*b*) Experimental test setup.

applied voltage, along the *y*-axis of the plate. The expansion of the actuator structure ultimately induces a curvature on the plate, as shown in Fig. 3. Specifically, Fig. 3(*a*) depicts the operation of the actuator schematically, while Figs. 3(*b*) and 3(*c*) show the experimental operation of the actuator. In this experiment, the actuation is either unpowered or is driven at a constant input voltage of 500 V: the first case will be denoted as "Actuator OFF," while the second case will be denoted as "Actuator ON."

To acquire the frequency response of the plate, two accelerometers, Isotron model 27AM1-10 and Dytran model 3255A1, are used to measure the transverse vibration of the tip and base of the plate, respectively. These signals are used to estimate the frequency response function (FRF) of the system between the tip acceleration and base acceleration of the plate due to the input excitation. Data acquisition is performed with a National Instruments USB-6341 DAQ card. For both the Actuator ON and Actuator OFF cases, 40 consecutive sweeps using an input chirp sine excitation with frequencies spanning 0.1–100 Hz, over a period of 10 s, are recorded. Note that, during the sweeps, the voltage of the bi-morph actuator is held constant. The shaker output signal amplitude is monitored to ensure that the plate is undergoing small amplitude vibrations and that the response of the system is linear. Data are acquired with a custom VI in LABVIEW with a sampling frequency of 2000 Hz. The FRF of the system is produced directly in the custom VI with the "Dual Channel Spectral Measurement" routine block. The FRFs obtained from each of the 40 runs are averaged and the results, for both Actuator ON and Actuator OFF cases, are displayed in Fig. 4.

The peak values in the FRF reveal the locations of the natural frequencies of the plate. The first prominent peak in the response, for both the Actuator ON and Actuator OFF case, is associated with a global cantilever-like first bending mode. We observe that the natural frequencies blue shift from 12.2 Hz to 12.8 Hz, demonstrating an increase of approximately 4.9% in the value of the first mode natural frequency. The error bars in the inset of Fig. 4 show ±1 standard deviation of the computed mean peak frequency values. Frequency shifts in the displayed spectrum can also be observed and ascribed to the imposed curvature from the bi-morph actuator. Via image analysis of pictures of the bent plate, we determine that the bi-morph actuator imposes a radius of curvature of

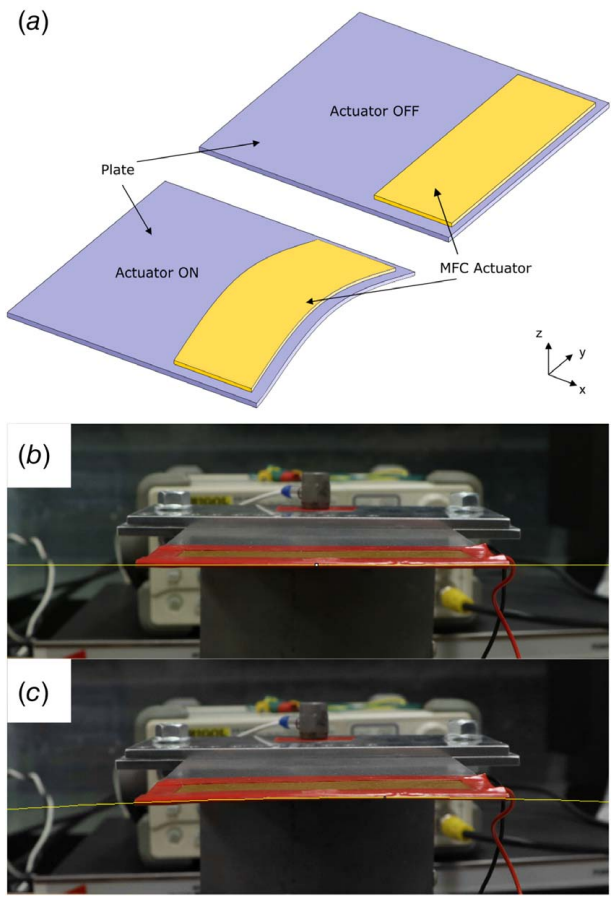

Fig. 3 (*a*) Schematic of the plate before ("Actuator OFF" case) and after actuation ("Actuator ON" case). Bending of the MFC actuator in the *yz*-plane produces the applied transverse curvature of the cantilevered plate. In (*b*) and (*c*), photos of the plate before and after actuation, respectively, with demonstration of the identification of the imposed curvature via image analysis.

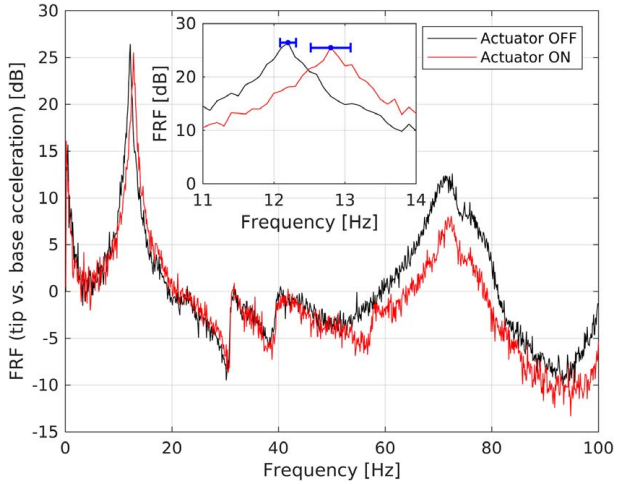

Fig. 4 Mean FRF between the cantilever plate tip and base excitation acceleration, for the Actuator ON and Actuator OFF cases. Error bars in the inset show ±1 standard deviation of the computed mean peak frequency values.

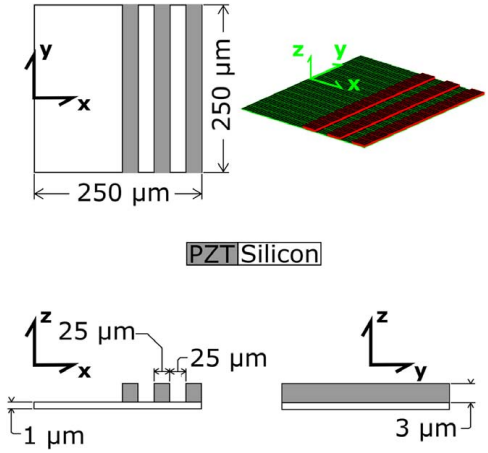

Fig. 5 Microscale device geometry used in the finite element analysis

approximately $R_c = 1192$ mm, which results in a nondimensional curvature parameter of $\kappa = b/R_c = 0.087$. Despite the modest value of the imposed curvature, the blue shift in natural frequency is significant and establishes a macroscale proof-of-concept for the tunability of AFM sensors via externally imposed curvature. In addition to the spectral blue shift, we note differences in the amplitude response of the two cases. Since the same drive is provided to the system in both cases, we expect that the amplitudes of the response in the Actuator ON case are to be decreased, as a consequence of the increased plate stiffness as predicted by the Theorema Egregium. This also assumes that the modal damping has remained constant.

3 A Proposal for Atomic Force Microscopy Application

In lieu of fabricating the proposed device at the microscale, suitable for AFM applications, we perform a three-dimensional finite element analysis (FEA) to study the device behavior. Here, we assume that lead zirconate titanate (PZT) actuators are used to control the device curvature. In the microsimulation, the main body of the sensor is composed of silicon with a Young's modulus of 169 GPa and Poisson's ratio of 0.25. The length and width of the plate have been chosen such that the aspect ratio (length/width) is 1. This aspect ratio increases the modal density of the system [24] and enhances the curvature stiffening effect [26], as compared to a thin, narrow beam geometry. The geometry chosen for the model can be found in Fig. 5 and PZT strip coefficients are reported in Table 2 in the Appendix. The PZT geometry and placement have been chosen in an attempt to maximize the device curvature in the desired direction while minimizing curvatures in competing directions.

Three-dimensional brick elements are used to mesh the silicon plate, and three-dimensional piezoelectric brick elements are used for the PZT strips. The edge of the plate at $x = 0$ is fixed such that there is no displacement or rotation. The remaining edges of the plate are free. The surfaces of the PZT elements normal to the xy-plane (see Fig. 5) and in contact with the silicon plate are given zero voltage boundary conditions. The top of the PZT elements, normal to the xy-plane, are given various input voltage values, depending on the simulation. In the simulations performed, sample contact is approximated by a linear spring and tip geometry is ignored. In the simulations, we study the tip location, for an aspect ratio 1 plate, which achieves optimal measurement sensitivity and modal density as determined by Aureli et al. [24]. This optimal location, henceforth called location A, is given by $x = 0.91\ L$ and $y = 0.4\ b$, where $x = 0$ is at the fixed end of the plate and $y = 0$ is at the centerline of the plate as depicted in Fig. 1(*a*). Here, consistent with Ref. [24], the sensitivity is defined as the rate of change of the contact resonance frequencies for a unit increase in the sample stiffness. The second tip location chosen for this study, and the next optimal, is at $x = 0.91\ L$ and $y = 0$ and will be referred to as location B. While in this paper we focus on the case of a purely elastic sample, viscoelasticity of the sample, relevant for biological applications, can be seamlessly introduced in the problem by following Aureli and Tung [27].

The numerical experiments are conducted in two distinct phases. In the first phase, an input voltage is applied to the PZT strips and an analysis is performed to determine the static equilibrium configuration of the device. We account for geometric nonlinearities introduced by large displacements and assume small strains and linear material elasticity. After the static input voltage is applied to the PZT strips, we observe a transverse curvature κ_x, a longitudinal curvature κ_y, and a deflection of the sensor in the z-direction. This deflection is dependent on the sign of the transverse curvature κ_x, which, in turn, is dependent on the sign of the voltage applied. This deflection must be accounted for in real-world AFM applications. After applying a static voltage, the static stiffness k_c of the sensor is then calculated for the deformed configuration. This is accomplished by applying a small load F, normal to the xy-plane of the undeformed plate, at the centerline ($x = L$ and $y = 0$) of the free end of the plate. The resulting static displacement d is then measured. The static stiffness is then calculated using $k_c = F/d$.

In the second phase of the numerical experiments, we apply an input voltage to the PZT strips and calculate the resulting static equilibrium configuration. We then perform a modal analysis using this equilibrium configuration for a given range of spring stiffnesses (including zero stiffness) attached at the aforementioned tip locations. These springs emulate contact with a measurement sample that would be experienced in actual contact resonance AFM experiments. Here, we have defined the nondimensional stiffness α as $\alpha = k/k_c^0$ where k is the assigned sample stiffness (linear spring) and k_c^0 is the static stiffness of the undeformed plate. Details regarding FEA convergence and chosen input voltage ranges can be found in the Appendix. In Sec. 4, we discuss the results of the FEA analysis.

4 Results and Discussion

4.1 Static Stiffness and Midpoint Deflection. Figure 6 shows the calculated static stiffness of the sensor versus input voltage to the piezoelectric strips. For a ±100 V input range, the static stiffness of the sensor is increased over 225%, with an absolute increase of

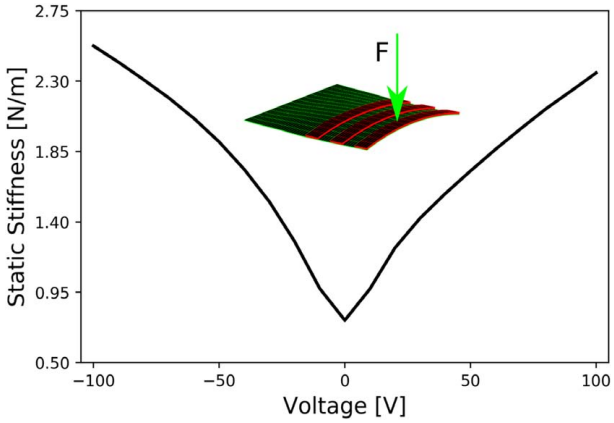

Fig. 6 Calculated static bending stiffness of the sensor versus voltage applied. The stiffness of the device is increased over 225% with an absolute increase of 1.75 N/m.

1.75 N/m. Slight asymmetry can be observed in the evolution of static stiffness for positive versus negative applied voltages. This asymmetry was predicted by Pini et al. [26] and Eq. (1) for plates undergoing longitudinal bending in a fixed direction. One can observe that the change in the stiffness, defined by Eq. (1), is dependent on the sign of the transverse curvature κ_x in the $\nu\kappa_x\kappa_y$ term of the equation. Additional stiffness asymmetry may have been introduced by placement of the piezoelectric strips on a single face of the plate.

Figure 7 shows the calculated midpoint deflection and nondimensional curvature κ of the sensor versus input voltage to the piezoelectric strips. Here, midpoint deflection measures the relative displacement between the centerline and free edges of the plate, as depicted in Fig. 7. A very small asymmetry can be observed in the midpoint deflection. This may be due to the assymmetric placement of the piezoelectric actuators and the nature of Eq. (1). The nondimensional curvature $\kappa = b/R_c$ has been calculated following the approach of Ahsan and Aureli [28], assuming that the curvature profile of the free end of the plate is circular. This assumption creates a direct relationship between the radius of curvature and the width of the plate given by $R_c\theta = b/2$, where θ is the sweep angle depicted in the lower right inset of Fig. 7. Next, the midpoint deflection δ is related to the radius of curvature and sweep angle by $R_c(1-\cos\theta) = \delta$. Using the first relationship to re-write θ in terms of κ and scaling by b, we obtain $(1/\kappa)(1-\cos(\kappa/2)) = \delta/b$. Rewriting the cosine function using a Maclaurin series and keeping terms up to second order leads to the relationship $\kappa \approx 8\delta/b$. The maximum nondimensional curvature observed in the simulations is approximately $\kappa = 0.5$, whereas the maximum nondimensional curvature observed in the proof-of-concept experiment was $\kappa = 0.087$, that is, approximately 17% of the total curvature applied in the simulations.

To verify the numerical simulations, a macroscale simulation is conducted using the geometry and material properties of the experimental proof-of-concept device. The length, width, and thickness of the macroscale plate are 104 mm, 104 mm, and 0.254 mm, respectively. The PZT strip has a length of 104 mm, a width of 10.4 mm, and a thickness of 0.764 mm. For simplicity, the PZT material and PZT placement are identical to the microscale simulation. A voltage of 660 V is applied to produce the same radius of static curvature found in the experiment, that is, 1192 mm. A natural frequency shift of approximately 5.2% (12.33–12.97 Hz) is found between the uncurved and curved configurations of the simulated device. The macroscale experiment showed a natural frequency shift of 4.7% (12.2–12.8 Hz). Minor differences in the uncurved natural frequencies of the experimental and simulation device are observed, most likely due to the PZT placement used in the simulation and minor differences in the simulated and actual material and geometric properties of the device.

4.2 Eigenfrequencies, Curve Veering, and Stiffness Sensitivity. In this section, we study how the natural frequencies of the sensor system vary with increasing applied curvature established via the voltage applied across the PZT strips. Robust tracking of the system's natural frequencies is necessary for proper sensor implementation. The sensor should be able to selectively tune its resonance amplification bandwidth, or dynamic stiffnesses, to the desired operating regimes.

The natural frequencies of the plate system are calculated via modal analysis. Figure 8 shows the system's natural frequencies as a function of the applied voltage. Each natural frequency has a unique mode shape associated with it and these shapes dictate the overall effect that the applied static curvature has on the dynamic stiffness. It is clear from Fig. 8 that each mode responds differently to the statically applied curvature. As seen from Fig. 8, all of the modes are affected by the induced curvature to some extent. The degree of change in the natural frequency for each mode depends on the mode shape the structure is operated at, and has been calculated through FEA. Some modes show a large change in their natural frequencies, while other exhibit very little change. By exploiting this idea, unaffected modes could be used as references for the undeformed configuration measurement data, whereas the affected modes could be used for resonance amplification or dynamic stiffness tuning purposes.

An additional complication arises as the device stiffness is increased, whereby the natural frequencies and mode shapes of

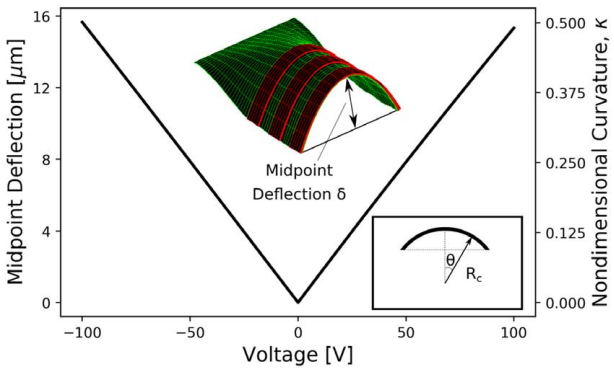

Fig. 7 Calculated midpoint deflection δ and nondimensional curvature κ of the sensor versus applied voltage. The deformation of the sensor in the inset pictures has been exaggerated for explanatory purposes.

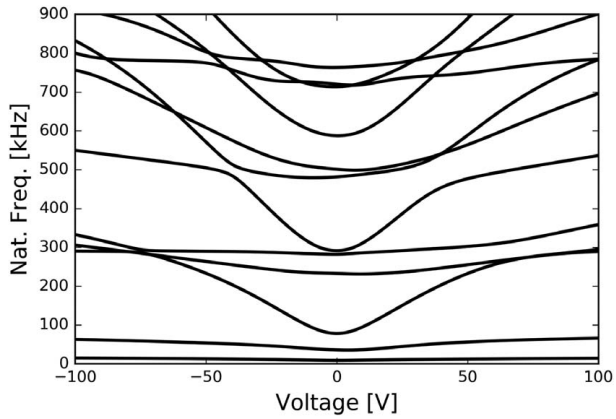

Fig. 8 Calculated natural frequencies of the sensor for various input voltages (applied curvatures). Complicated crossing and veering behavior of the natural frequencies can be observed throughout.

the system interact with each other when in close frequency proximity. As the natural frequency loci approach one another in frequency space, they can either cross or veer. Natural frequency crossing [29,30] is a phenomenon that takes place when the trajectories of natural frequency loci intersect while one or more system parameters are varied. During natural frequency crossing, the mode shapes of each natural frequency remain unchanged. On the other hand, natural frequency veering [31–40] is a phenomenon where two natural frequencies approach one another and abruptly change trajectories without crossing or intersecting. Each natural frequency then follows the trajectory previously taken by the other before the veering event. The mode shapes change violently as they continuously veer. This behavior has been described by Leissa [37]—"figuratively speaking, a dragonfly one instant, a butterfly the next, and something indescribable in between." Natural frequency curve veering, initially regarded as an anomaly occurring as a result of numerical discretization of continuous systems, has been proven to be a real phenomenon via perturbation methods for both discrete and continuous systems [40,41].

In order to study the effect that curvature-based stiffening has on the natural frequencies and mode shapes of the plate system, we must first be able to track mode shapes of interest through veering or crossing events in a robust way. In this paper, we adapt the method of "eigenfunction sensitivity" used by Huang et al. [42] to robustly track natural frequencies and mode shapes of interest. We define the eigenfunction sensitivity between the rth and sth mode S_{rs} as the inner product:

$$S_{rs} = |\hat{\phi}_r^T \hat{\phi}_s^0| \tag{2}$$

where $\hat{\phi}_s^0$ is a column vector representing the sth normalized mode shape of the unperturbed flat plate, $\hat{\phi}_r$ is a column vector representing the rth normalized mode shape of the plate at a voltage of interest, and vertical bars denote absolute value. Since no analytical approach is available to predict the mode shapes for the proposed plates, the ϕ vectors are, as customary, the eigenvectors of the numerical modal analysis problem solved in the FEA. The mode shape normalization has been defined as $\hat{\phi}_s^0 = \frac{\phi_s^0}{||\phi_s^0||}$ and $\hat{\phi}_r = \frac{\phi_r}{||\phi_r||}$, where $||\bullet|$ is the vector L2 norm. The value of S_{rs} varies between 0 and 1, so that for S_{rs} values of 1, the compared modes look identical, while for S_{rs} values of 0, the mode shapes are orthogonal. When comparing mode shapes that cross, the eigenfunction sensitivity will display a jump discontinuity. For veering modes, the S_{rs} will change in a continuous fashion throughout the veering region [42].

Figure 9(*a*) depicts a representative region of interest where crossing and veering behavior is observed. Here, ϕ_3, ϕ_4, and ϕ_5 represent an ordered set of calculated mode shapes/natural frequencies. Nonphysical kinks can be observed in the natural frequency as a function of the voltage plot in Fig. 9(*a*) for ϕ_3 as the negative voltage applied to the plate increases. Clearly, ϕ_3 and ϕ_4 cross near −70 V and again near −80 V. Figure 9(*b*) elucidates this crossing behavior. As we calculate the eigenfunction sensitivity of ϕ_3 with its unperturbed state ϕ_3^0, given by S_{33}, we see two jump discontinuities near −70 V and −80 V. The eigenfunction sensitivity drops to zero between −70 V and −80 V, indicating that ϕ_3 is orthogonal to its unperturbed shape in this domain. This is a result of modal crossing. The complementary behavior can be observed in S_{34}.

Veering behavior can also be observed in Fig. 9(*a*) between two modes. ϕ_5 can be observed to sharply change trajectories near −75 V. The eigenmode sensitivity S_{53} gradually changes in the veering region. Note that S_{35} would be equivalent to S_{53} if no extraneous modes crossed and the veering existed in isolation. The complementary behavior can be seen in S_{33} and S_{34}, accounting for the aforementioned mode crossing.

Starting from the zero voltage case, we calculate the eigenmode sensitivity of a mode of interest with its unperturbed state and the eigenmode sensitivity of the unperturbed mode of interest and any nearby frequencies for which a crossing or veering is suspected

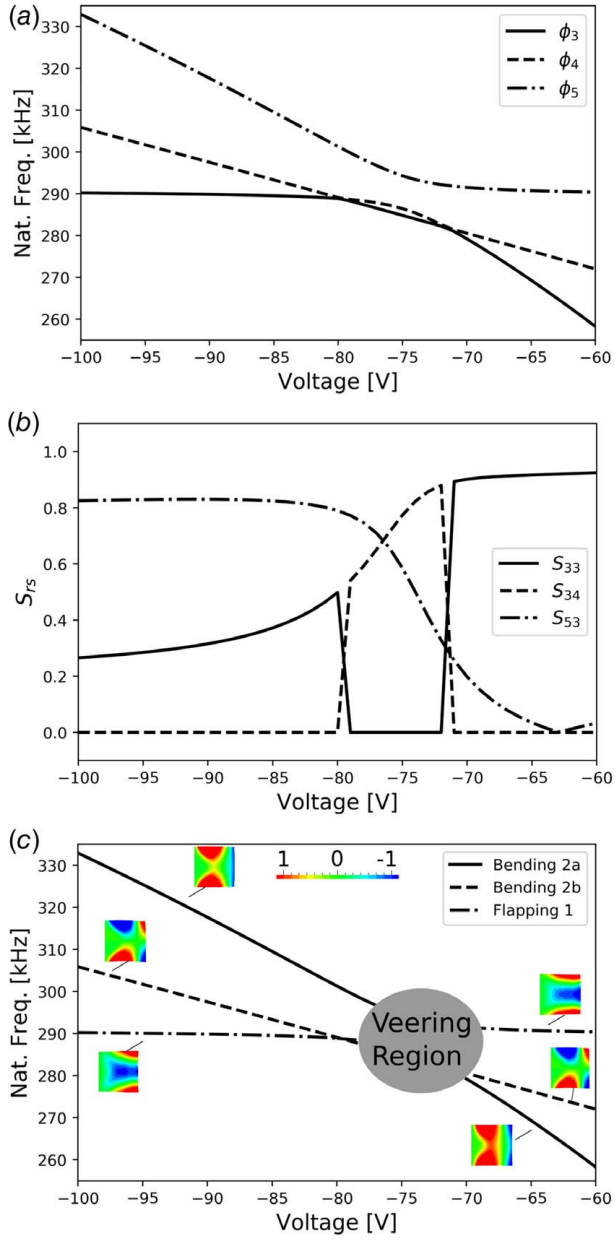

Fig. 9 (*a*) Behavior of natural frequency for three numerically ordered modes versus applied voltage (applied curvature) showing crossing and veering. (*b*) Eigenfunction sensitivity S_{rs} used to discriminate between modal crossing and modal veering. (*c*) Robustly "tracked" mode shapes. Bending mode 2a and flapping mode 1 have effectively swapped positions after veering, whereas bending mode 2b has remained on its original trajectory. Inset pictures depict the eigenmodes of vibration at the locations indicated.

(the complementary eigenmode sensitivity may be used if crossings exist). In Fig. 9(*c*), we track the second bending mode of vibration with in-phase bending behavior, named "Bending 2a." At each successive increase in voltage, our tracking algorithm assigns the identifier "Bending 2a" to the frequency value that has the highest eigenmode sensitivity in relation to the unperturbed bending mode 2a and has a monotonically increasing frequency value. That is, modal frequencies should not decrease as the sensor stiffness is increased. However, the curve veering phenomenon could decrease the frequency of an eigenmode as the participating modes exchange their place in the frequency domain. In Fig. 9, we see that, after veering, flapping mode 1 swaps places with bending mode 2a, and

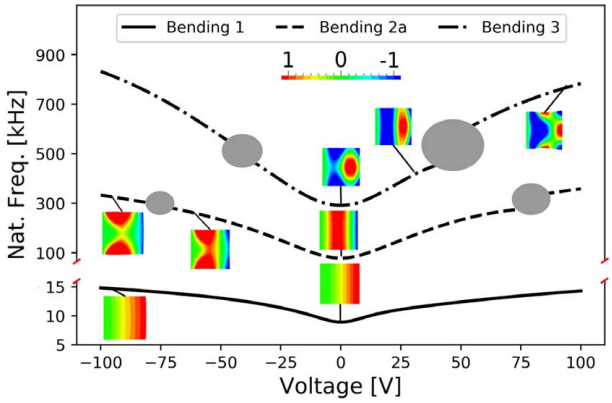

Fig. 10 Corrected natural frequencies of the sensor for various input voltages (applied curvatures). Veering regions are indicated with gray ovals. Note the broken *y*-axis to enhance the contrast of mode 1.

Table 1 Calculated natural frequencies versus applied PZT voltage for bending mode 1, bending mode 2a, and bending mode 3

Voltage (V)	B1 (kHz)	B2a (kHz)	B3 (kHz)
−100	14.81	332.91	832.41
−75	14.06	286.46	722.34
−50	13.04	233.22	571.38
−25	11.39	150.61	393.29
0	8.90	78.19	291.55
25	11.08	150.35	386.66
50	12.38	232.60	476.73
75	13.43	276.32	704.31
100	14.28	358.55	783.64

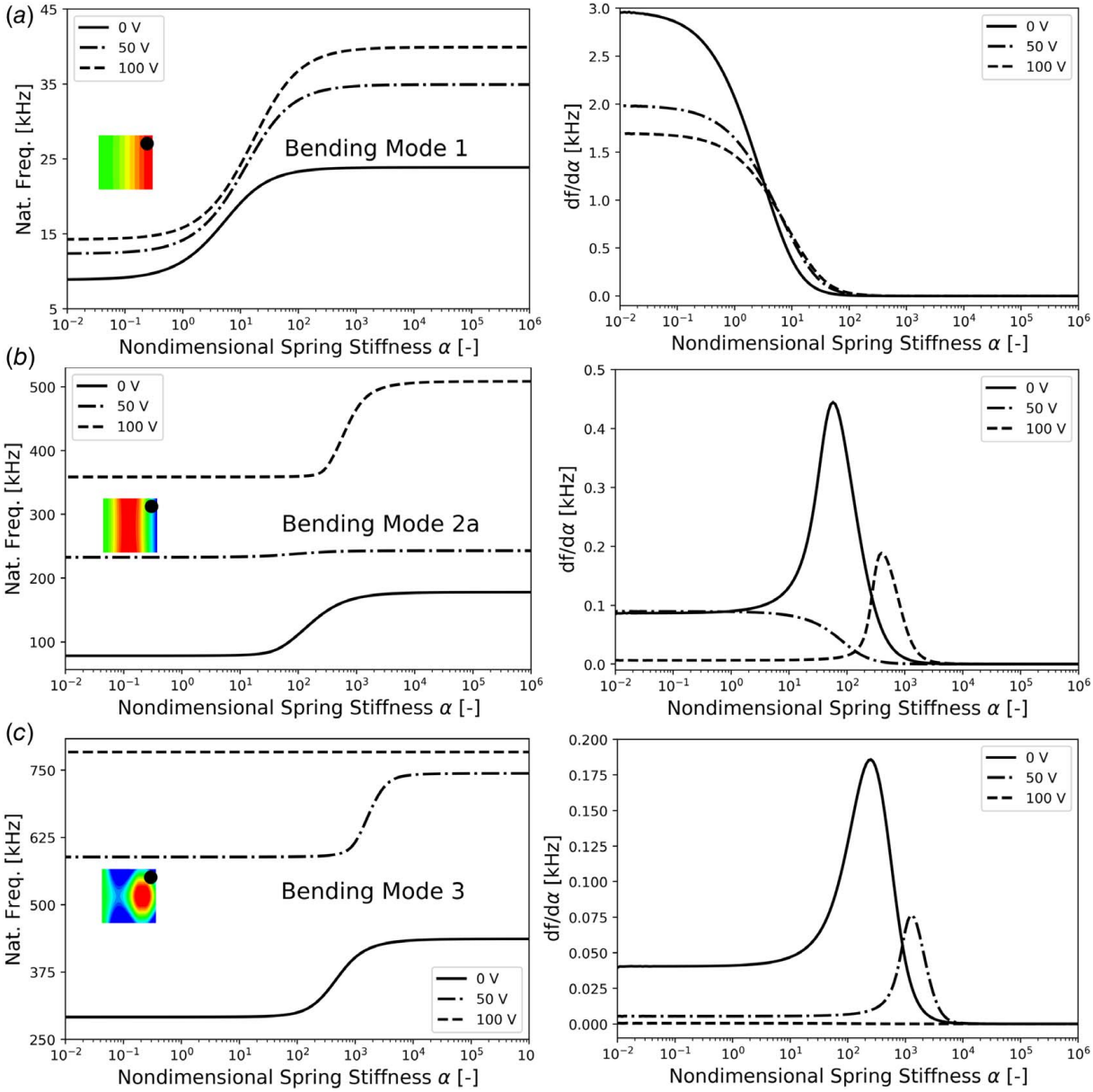

Fig. 11 Natural frequencies and natural frequency stiffness sensitivities versus sample stiffness for various PZT voltages for tip location A. Inset images depict the eigenmodes of vibration at 0 V. The spring location is indicated by the black dot in the inset images.

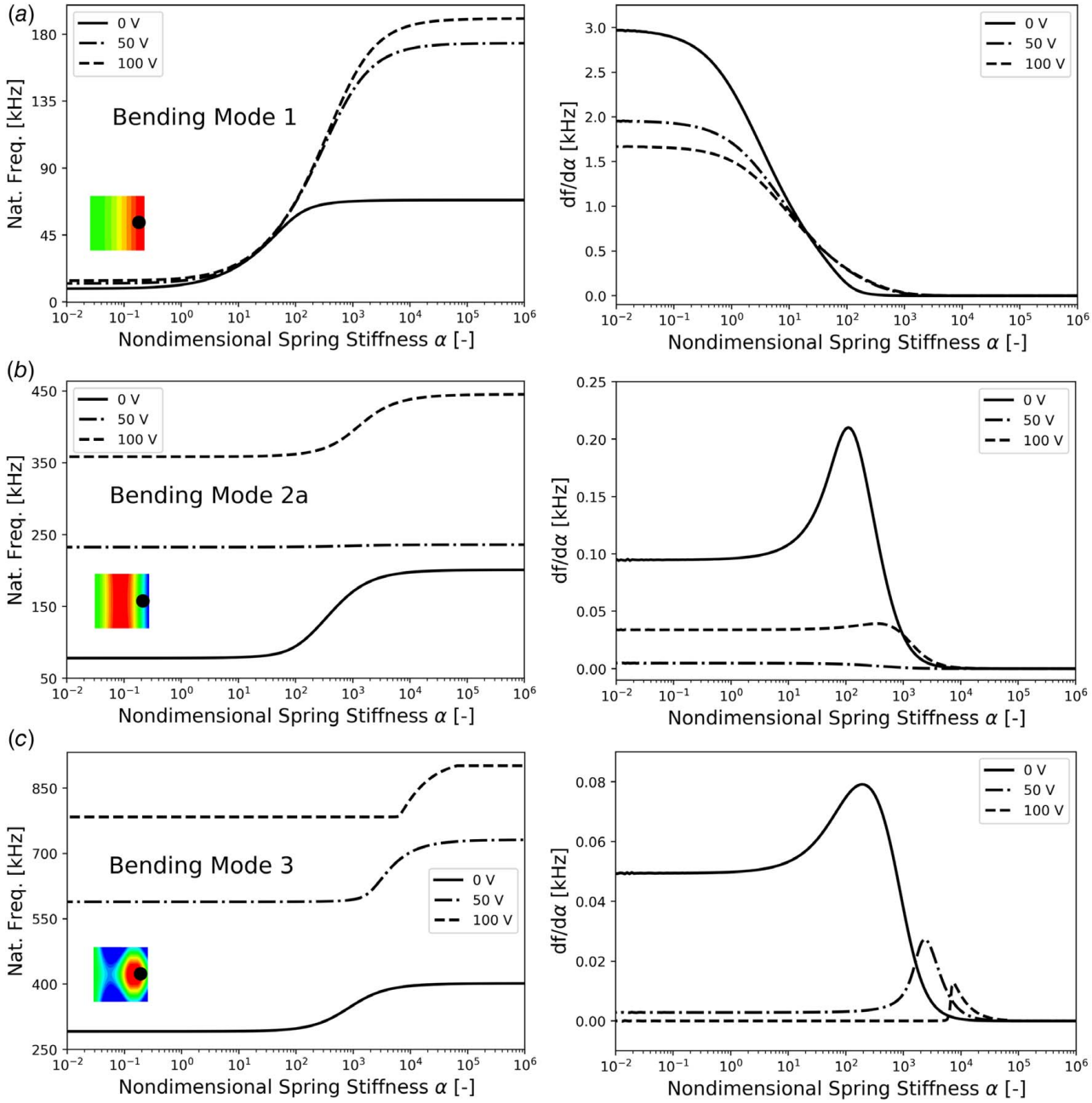

Fig. 12 Natural frequencies and natural frequency stiffness sensitivities versus sample stiffness for various PZT voltages for tip location B. Inset images depict the eigenmodes of vibration at 0 V. The spring location is indicated by the black dot in the inset images.

thus the frequency of flapping mode 1 decreases. Additionally, when the eigenfunction sensitivities of two veering modes r and s, relative to mode s (or equivalently r), are comparable, that is $|S_{ss} - S_{rs}| \leq 0.1$, the tracking algorithm does not attempt to discriminate between modes. These regions are denoted as "veering regions"

Figure 9(*c*) shows the robustly tracked mode shapes using the eigenfunction sensitivity technique. The inset figures in Fig. 9(*c*) depict the out-of-plane displacements of the mode shape associated with the indicated curves. For all inset mode shape pictures, the left side of the picture represents the fixed boundary side. As seen in Fig. 9(*a*), the natural frequency locus of ϕ_5 varies continuously and does not intersect the neighboring natural frequency loci curves. However, the modal behavior of ϕ_5 drastically changes after veering as observed in the modal insets of Fig. 9(*c*). In order to successfully operate the proposed curvature stiffening sensor, veering and crossing regions must be successfully identified, and experimental procedures to compensate for these phenomena must be developed.

Figure 10 shows the tracked mode shapes of the first three bending modes of vibration for the system. Following the eigenfunction sensitivity method put forward in this paper, it should be possible to experimentally track eigenmodes of interest in real-world AFM applications using systems equipped with scanning lasers [43]. In this way, arbitrary tuning of resonance amplification and dynamic stiffness will be experimentally possible.

Examining Fig. 10, we see that bending mode 1 displays a maximum frequency change of approximately 67%, bending mode 2a displays a maximum frequency change of approximately 350%, and bending mode 3 displays a maximum frequency change of approximately 185% for the voltage range tested. Table 1 shows the calculated natural frequency changes for the first three bending modes as a function of applied PZT voltage. The range of frequency

shifts observed in the simulations are promising and indicate the feasibility of the proposed sensor.

In order to use the proposed sensor in the context of contact resonance atomic force microscopy (CR-AFM), we study the effect of natural frequency change and natural frequency stiffness sensitivity $\mathrm{d}f/\mathrm{d}\alpha$ as a function of sample stiffness and applied voltage. For this study, we have selected two "optimal tip" locations as defined by Aureli et al. [24]. These two tip positions roughly correspond to the distal end of the cantilevered plate at the center and the edge and are given explicitly in the preceding text (location A at $x=0.91\ L$, $y=0.4\ b$ and location B at $x=0.91\ L$ and $y=0$). Sample stiffness is represented by a single linear spring in the z-direction. The natural frequency and natural frequency sensitivity have been calculated for nondimensional stiffness ranges of $\alpha=10^{-2}$ to $\alpha=10^{6}$, where $\alpha=k/k_c^0$, k is the assigned sample stiffness and k_c^0 is the static stiffness of the undeformed plate.

Figures 11 and 12 show the natural frequencies and natural frequency stiffness sensitivity versus sample stiffness for three applied PZT voltages (0, 50 V, and 100 V) for three bending modes of the system at the optimal sensor tip locations. It is clear from the natural frequency data in panels (a)–(c) that the applied voltage (sensor curvature) can be used to effectively tune the natural frequency of the device across a wide range of frequencies and sample stiffnesses. This effect can be used to selectively tune the sensor to achieve resonance amplification at desired frequencies, for a given sample stiffness. Additionally, we see that the effective stiffness detection range, for each bending mode, can be increased with applied curvature. For example, in Fig. 12(*a*) we see that, for bending mode 1 at 0 V, the stiffness detection limit is approximately at $\alpha=200$. Above this nondimensional stiffness, the device frequency shows no further increase with increasing stiffness. However, at applied curvatures using PZT voltages of 50 V and 100 V, the stiffness detection range is extended well above $\alpha=1000$.

We also see from Figs. 11 and 12 that the optimal sensing tip location A does indeed have increased sensitivity as compared to location B, as defined by the metric in Aureli et al. [24], for the 0 V case. However, as the voltage is increased, the optimal tip location is expected to change position. In future studies, we would like to explore the evolution of optimal tip location for a given device curvature. Additionally, as seen in Fig. 11(*c*), it is possible for the tip location to coincide with a nodal vibration line and reduce the stiffness sensitivity to zero. This is observed in the 100 V actuation case for bending mode 3 at tip location A. The 50 V actuation case for bending mode 2a at tip location B appears to be near a nodal line and displays a sensitivity near zero.

Finally, as the sensor stiffness is increased, the overall stiffness sensitivity $\mathrm{d}f/\mathrm{d}\alpha$ of each bending mode decreases with respect to its less stiff, unperturbed counterpart. This is expected, and it is predicted by a simple one-dimensional lumped-parameter model. Let the natural vibration frequency be given by $f=\frac{1}{2\pi}\sqrt{\frac{k_{\mathrm{eff}}}{m_{\mathrm{eff}}}}$, where k_{eff} and m_{eff} are the effective stiffness and mass of the lumped-parameter model. Then, the frequency sensitivity with respect to stiffness is given by $\frac{\mathrm{d}f}{\mathrm{d}k_{\mathrm{eff}}}=\frac{1}{4\pi}\sqrt{\frac{1}{m_{\mathrm{eff}}}}\sqrt{\frac{1}{k_{\mathrm{eff}}}}$. As the effective stiffness or mass of the system increases, the frequency sensitivity to stiffness decreases.

Real-world implementation of this sensor may require an updated technique to measure the system response. The traditional optical lever technique used in AFM may be sufficient, so long as the light scattering effect due to the induced curvature is not too great. Additionally, a calibration must be performed to quantify the resulting parasitic displacement that results from applying a static curvature. Extracting a sensing signal from the actuating material may also be used to measure the system's response.

5 Conclusions

In this work, we have presented the idea of curvature-based resonance and stiffness adjustment for AFM applications. A proof-of-concept macroscale experiment is first presented, followed by a finite element analysis of the microscale sensor. We observe that applied transverse curvature is an effective method to change the static stiffness and natural frequencies of a microplate sensor. Additionally, an eigenfunction sensitivity method is presented to effectively track the mode shapes of the system as the system stiffness is increased and natural frequency curve veering and curve crossing are encountered. The characterization of some frequency-dependent materials using CR-AFM may be challenging due to the limitation of the sensitivity of the AFM probe used to investigate the material. A tunable sensor probe, that has the capability to be optimized according to the sample, could improve the accuracy of the estimation of nanomechanical properties. A frequency-tunable sensor also has numerous potential applications in the field of nanometrology. We believe this work represents a fundamental and necessary step toward the creation of a real-world curvature stiffening-based microsensor.

Acknowledgment

This material is based in part upon work supported by the National Science Foundation under grant CMMI-1660448 (to RCT) and grant CMMI-1847513 (to MA). The authors would like to thank Navid Forootan for his help with the experiments.

Conflict of Interest

There are no conflicts of interest.

Appendix

Finite Element Analysis Convergence. Mesh convergence is determined by examining the following three parameters: (i) the first eigenfrequency of the system, (ii) the static tip displacement of the sensor due to plate curvature, and (iii) the static tip displacement due to an applied normal load. Mesh convergence is considered to be achieved when each of these parameters changes less than 0.25% after doubling the number of elements for two consecutive reductions when applying a 100 V input voltage. The number of mesh subdivisions was converged at 50, 11, and 7 for length, width, and thickness plate subdivisions, respectively. The piezoelectric strip achieved convergence at 5 subdivisions along its length, 11 width subdivisions, and 7 thickness subdivisions. Meshing is performed using ADINA software [44], with 27 nodes per element and mapped or rule-based meshing. Mesh convergence is achieved at 3850 solid elements for the plate and 385 solid elements for each piezoelectric strip.

Lead Zirconate Titanate Coefficients. The stress and strain response of the lead zirconate titanate (PZT) material extensively depends on its piezoelectric and dielectric properties. These properties are dependent on factors such as manufacturing techniques, grain size, film thickness and orientation, operating temperature, operating time, operating voltage, and the dimensions and geometry

Table 2 PZT strip coefficients and material properties. Subscripts represent the material coordinate system, where 1 = x, 2 = y, 3 = z, 4 = xy, 5 = xz, and 6 = yz

Stress coefficient (N/Vm)	Strain coefficient (m/V)	Young's modulus (GPa)	Poisson's ratio (–)	Shear modulus (GPa)
e_{13} −7.21	d_{13} −1.85*E*-10	E_1 61	ν_{12} 0.35	G_{12} 22.6
e_{23} −7.21	d_{23} −1.85*E*-10	E_2 61	ν_{13} 0.38	G_{13} 21.1
e_{33} 15.12	d_{33} 3.87E-10	E_3 53.2	ν_{23} 0.38	G_{23} 21.1
e_{51} 12.33	d_{51} 5.84E-10			
e_{62} 12.33	d_{62} 5.84E-10			

of the material [45–48]. It is challenging to predict the PZT material properties (i.e. piezoelectric stress and strain coefficients) without proper experimental study. In this work, we have used values for bulk PZT materials, although PZT thin films (thickness <10 μm) may have properties that differ from bulk values. The piezoelectric stress and strain coefficients change nonlinearly as the transition occurs from a PZT thick film to a thin film. In most cases, a dedicated experimental setup is required to ensure the fidelity of the specific piezoelectric coefficients. Guo et al. [45] introduced a calibration factor to compare the impact of theoretical piezoelectric strain coefficients on the basis of substrate materials, boundary conditions, specimen size, thickness ratio, and specimen thickness with the experimental values. The largest deviation (250% increase) in the calibration factor found was due to the change in the thickness ratio (where the substrate thickness to PZT thickness ratio was 1:0.0029). The impact of the other parameters was not significant (less than 7%). For the FEA study in this work, the silicon substrate to PZT thickness ratio is 1:3 so that the calibration factor/deviation of the strain coefficient from the experimental values becomes insignificant, and the bulk property values of PZT can be used during the simulation.

The maximum applicable bias voltage applied to the PZT thin films is another area of study that depends on the dielectric breakdown strength of the material. Ko et al. [49] reported improved dielectric breakdown strength of PZT films by decreasing the proportion of excess oxide layers. These oxide layers are responsible for increasing the leakage current, which leads to a drop in dielectric breakdown strength of the PZT material. Ko et al. achieved dielectric breakdown strengths of 300 kV/cm to about 1 MV/cm. For the FEA simulations performed in this work, the dielectric breakdown strength is assumed to be 333 kV/cm. This enables a PZT input voltage range of -100 V to $+100$ V across the 3 μm thick PZT strips.

References

[1] Gurrum, S. P., King, W. P., Joshi, Y. K., and Ramakrishna, K., 2008, "Size Effect on the Thermal Conductivity of Thin Metallic Films Investigated by Scanning Joule Expansion Microscopy," ASME J. Heat. Transfer., **130**(8), p. 082403.

[2] Song, J., Lu, C., Xie, X., Li, Y., Zhang, Y., Grosse, K. L., Dunham, S., Huang, Y., King, W. P., and Rogers, J. A., 2013, "Thermomechanical Modeling of Scanning Joule Expansion Microscopy Imaging of Single-Walled Carbon Nanotube Devices," ASME J. Appl. Mech., **80**(4), p. 040907.

[3] Deniset-Besseau, A., Prater, C. B., Virolle, M., and Dazzi, A., 2014, "Monitoring TriAcylGlycerols Accumulation by Atomic Force Microscopy Based Infrared Spectroscopy in Streptomyces Species for Biodiesel Applications," J. Phys. Chem. Lett., **5**(4), pp. 654–658.

[4] Balke, N., Bdikin, I., Kalinin, S. V., and Kholkin, A. L., 2009, "Electromechanical Imaging and Spectroscopy of Ferroelectric and Piezoelectric Materials: State of the Art and Prospects for the Future," J. Am. Ceram. Soc., **92**(8), pp. 1629–1647.

[5] Luchkin, S. Y., Romanyuk, K., Ivanov, M., and Kholkin, A. L., 2015, "Li Transport in Fresh and Aged $LiMn_2O_4$ Cathodes Via Electrochemical Strain Microscopy," J. Appl. Phys., **118**(7), p. 072016.

[6] Amanieu, H.-Y., Thai, H. N., Luchkin, S. Y., Rosato, D., Lupascu, D. C., Keip, M.-A., Schröder, J., and Kholkin, A. L., 2015, "Electrochemical Strain Microscopy Time Spectroscopy: Model and Experiment on $LiMn_2O_4$," J. Appl. Phys., **118**(5), p. 055101.

[7] Yang, S., Wu, J., Yan, B., Li, L., Sun, Y., Lu, L., and Zeng, K., 2017, "Nanoscale Characterization of Charged/Discharged Lithium-Rich Thin Film Cathode by Scanning Probe Microscopy Techniques," J. Power. Sources, **352**, pp. 9–17.

[8] Rabe, U., and Arnold, W., 1994, "Acoustic Microscopy by Atomic-Force Microscopy," Appl. Phys. Lett., **64**(12), pp. 1493–1495.

[9] Hurley, D. C., Kopycinska-Muller, M., and Kos, A. B., 2007, "Mapping Mechanical Properties on the Nanoscale Using Atomic-Force Acoustic Microscopy," J. Minerals, Metals Mater. Soc., **59**(1), pp. 23–29.

[10] Killgore, J. P., Yablon, D. G., Tsou, A. H., Gannepalli, A., Yuya, P. A., Turner, J. A., Proksch, R., and Hurley, D. C., 2011, "Viscoelastic Property Mapping With Contact Resonance Force Microscopy," Langmuir, **27**(23), pp. 13983–13987.

[11] Rezaei, E., and Turner, J. A., 2017, "Contact Resonance AFM to Quantify the In-Plane and Out-of-Plane Loss Tangents of Polymers Simultaneously," Appl. Phys. Lett., **110**(10), p. 101902.

[12] Gonzalez-Martinez, J. F., Kakar, E., Erkselius, S., Rehnberg, N., and Sotres, J., 2019, "Effect of Relative Humidity on the Viscoelasticity of Thin Organic Films Studied by Contact Thermal Noise AFM," Langmuir, **35**(18), pp. 6015–6023.

[13] Fiedler-Higgins, C. I., Cox, L. M., DelRio, F. W., and Killgore, J. P., 2019, "Monitoring Fast, Voxel-Scale Cure Kinetics Via Sample-Coupled-Resonance Photorheology," Small Methods, **3**(2), p. 1800275.

[14] Killgore, J. P., Deolia, A., Robins, L., and Murray, T. W., 2019, "Experimental Reconstruction of the Contact Resonance Shape Factor for Quantification and Amplification of Bias-Induced Strain in Atomic Force Microscopy," Appl. Phys. Lett., **114**(13), p. 133108.

[15] Jesse, S., Mirman, B., and Kalinin, S. V., 2006, "Resonance Enhancement in Piezoresponse Force Microscopy: Mapping Electromechanical Activity, Contact Stiffness, and Q Factor," Appl. Phys. Lett., **89**(2), p. 022906.

[16] Kofahl, C., Güthoff, F., and Eckold, G., 2019, "Direct Observation of Polar Nanodomains in the Incommensurate Phase of $(K_0.96Rb_0.04)_2ZnCl_4$ Crystals Using Piezo Force Microscopy," Ferroelectrics, **540**(1), pp. 10–17.

[17] Zhu, Q., Pan, K., Xie, S., Liu, Y., and Li, J., 2019, "Nanomechanics of Multiferroic Composite Nanofibers Via Local Excitation Piezoresponse Force Microscopy," J. Mech. Phys. Solids., **126**, pp. 76–86.

[18] Zine-El-Abidine, I., and Yang, P., 2009, "A Tunable Mechanical Resonator," J. Micromech. Microeng., **19**(12), p. 125004.

[19] Mueller-Falcke, C., Song, Y.-A., and Kim, S.-G., 2004, "Tunable Stiffness Scanning Microscope Probe," Optics East, Philadelphia, PA, SPIE, pp. 31–37.

[20] Mueller-Falcke, C., Gouda, S. D., Kim, S., and Kim, S.-G., 2006, "A Nanoscanning Platform for Bio-Engineering: An In-plane Probe With Switchable Stiffness," Nanotechnology, **17**(4), p. S69.

[21] Syms, R. R. A., 1998, "Electrothermal Frequency Tuning of Folded and Coupled Vibrating Micromechanical Resonators," J. Microelectromech. Syst., **7**(2), pp. 164–171.

[22] Zhang, H. J., and Qiu, C. J., 2006, "Characterization and MEMS Application of Low Temperature TiNi(Cu) Shape Memory Thin Films," Mater. Sci. Eng. A., **438**, pp. 1106–1109.

[23] Kawai, Y., Ono, T., Meyers, E., Gerber, C., and Esashi, M., 2006, "Piezoelectric Actuator Integrated Cantilever With Tunable Spring Constant for Atom Probe," 19th IEEE International Conference on Micro Electro Mechanical Systems, MEMS 2006, Istanbul, pp. 778–781.

[24] Aureli, M., Ahsan, S. N., Shihab, R. H., and Tung, R. C., 2018, "Plate Geometries for Contact Resonance Atomic Force Microscopy: Modeling, Optimization, and Verification," J. Appl. Phys., **124**(1), p. 014503.

[25] Gauss, C. F., 1902, *General Investigations of Curved Surfaces of 1827 and 1825*, Princeton University Library.

[26] Pini, V., Ruz, J. J., Kosaka, P. M., Malvar, O., Calleja, M., and Tamayo, J., 2016, "How Two-Dimensional Bending Can Extraordinarily Stiffen Thin Sheets," Sci. Rep., **6**(1), pp. 1–6.

[27] Aureli, M., and Tung, R., 2021, "A Plate-Like Sensor for the Identification of Sample Viscoelastic Properties Using Contact Resonance Atomic Force Microscopy," ASME Lett. Dyn. Syst. Controls, **1**(3), p. 031008.

[28] Ahsan, S. N., and Aureli, M., 2017, "Nonlinear Oscillations of Shape-Morphing Submerged Structures: Control of Hydrodynamic Forces and Power Dissipation Via Active Flexibility," J. Fluids Struct., **74**, pp. 35–52.

[29] Balmes, E., 1993, "High Modal Density, Curve Veering, Localization—A Different Perspective on the Structural Response," J. Sound Vib., **161**(2), pp. 358–363.

[30] Gallina, A., Pichler, L., and Uhl, T., 2011, "Enhanced Meta-Modelling Technique for Analysis of Mode Crossing, Mode Veering and Mode Coalescence in Structural Dynamics," Mech. Syst. Signal Process., **25**(7), pp. 2297–2312.

[31] Pierre, C., 1988, "Mode Localization and Eigenvalue Loci Veering Phenomena in Disordered Structures," J. Sound. Vib., **126**(3), pp. 485–502.

[32] Warburton, G., 1954, "The Vibration of Rectangular Plates," Proc. Inst. Mech. Eng., **168**(1), pp. 371–384.

[33] Mindlin, R., and Deresiewicz, H., 1954, "Thickness-Shear and Flexural Vibrations of a Circular Disk," J. Appl. Phys., **25**(10), pp. 1329–1332.

[34] Petyt, M., and Fleischer, C., 1971, "Free Vibration of a Curved Beam," J. Sound. Vib., **18**(1), pp. 17–30.

[35] Claassen, R., and Thorne, C., 1961, "Vibrations of Thin Rectangular Isotropic Plates," ASME J. Appl. Mech., **28**(2), pp. 304–305.

[36] Afolabi, D., and Mehmed, O., 1994, "On Curve Veering and Flutter of Rotating Blades," ASME. J. Eng. Gas Turbines Power, **116**(3), pp. 702–708.

[37] Leissa, A. W., 1974, "On a Curve Veering Aberration," Z. Angewandte Math. Phys. ZAMP, **25**(1), pp. 99–111.

[38] Nair, P., and Durvasula, S., 1973, "On Quasi-Degeneracies in Plate Vibration Problems," Int. J. Mech. Sci., **15**(12), pp. 975–986.

[39] Kuttler, J., and Sigillito, V., 1981, "On Curve Veering," J. Sound Vib., **75**(4), pp. 585–588.

[40] Perkins, N., and Mote Jr, C., 1986, "Comments on Curve Veering in Eigenvalue Problems," J. Sound. Vib., **106**(3), pp. 451–463.

[41] du Bois, J. L., Adhikari, S., and Lieven, N. A., 2007, "Experimental and Numerical Investigation of Mode Veering in a Stressed Structure," Proceedings of the 25th International Modal Analysis Conference, Orlando, FL, Feb. 19–22.

[42] Huang, J., Krousgrill, C. M., and Bajaj, A. K., 2006, "Modeling of Automotive Drum Brakes for Squeal and Parameter Sensitivity Analysis," J. Sound. Vib., **289**(1–2), pp. 245–263.

[43] Wagner, R., Killgore, J. P., Tung, R. C., Raman, A., and Hurley, D. C., 2015, "Vibrational Shape Tracking of Atomic Force Microscopy Cantilevers for Improved Sensitivity and Accuracy of Nanomechanical Measurements," Nanotechnology, **26**(4), p. 045701.

[44] ADINA R&D Inc., 2018. *ADINA 9.4 Manuals*. www.adina.com, Watertown, MA.

[45] Guo, Q., Cao, G., and Shen, I., 2013, "Measurements of Piezoelectric Coefficient $D_3$3 of Lead Zirconate Titanate Thin Films Using a Mini Force Hammer," ASME J. Vib. Acoust., **135**(1), p. 011003.
[46] Haccart, T., Cattan, E., and Remiens, D., 2002, "Dielectric, Ferroelectric and Piezoelectric Properties of Sputtered PZT Thin Films on Si Substrates: Influence of Film Thickness and Orientation," Semiconductor Phys. Quant. Electron. Optoelectron., **5**(1), pp. 78–88.
[47] Kurchania, R., and Milne, S., 1999, "Characterization of Sol-Gel $Pb(Zr_0.53Ti_0.47)O_3$ Films in the Thickness Range 0.25–10 μm," J. Mater. Res., **14**(5), pp. 1852–1859.
[48] Nam, H.-J., Kim, H.-H., and Lee, W.-J., 1998, "The Effects of the Preparation Conditions and Heat-Treatment Conditions of $Pt/Ti/SiO_2/Si$ Substrates on the Nucleation and Growth of $Pb(Zr, Ti)O_3$ Films," Jpn. J. Appl. Phys., **37**(6R), p. 3462.
[49] Ko, S. W., Zhu, W., Fragkiadakis, C., Borman, T., Wang, K., Mardilovich, P., and Trolier-McKinstry, S., 2019, "Improvement of Reliability and Dielectric Breakdown Strength of Nb-Doped Lead Zirconate Titanate Films Via Microstructure Control of Seed," J. Am. Ceram. Soc., **102**(3), pp. 1211–1217.